CrossMark

Decadal changes in the Southern Hemisphere sea surface temperature in association with El Niño–Southern Oscillation and Southern Annular Mode

Sae-Rim Yeo · Kwang-Yul Kim

Abstract The spatial structure of El Niño–Southern Oscillation (ENSO) and the Southern Annular Mode (SAM), which are the two most important climate modes affecting sea surface temperature (SST) variability in the Southern Hemisphere (SH), appear to have changed since 1999. The characteristic features of the ENSO- and SAM-related atmospheric and oceanic variability in the SH are compared between two sub-periods (1979–1998 and 1999–2012) using cyclostationary empirical orthogonal function analysis. During the earlier period of 1979–1998, the ENSO is characterized by conventional eastern Pacific type, in which the signals in the SH constitute the Pacific South America teleconnection pattern. In contrast, due to a shift of the active center of ENSO to the central Pacific in the later period (1999–2012), atmospheric circulation and SST variability over the SH significantly vary. Moreover, the SAM-related SST variability also shows remarkable differences before and after 1998–1999. This difference is primarily attributed to differences in the non-annular spatial component of the SAM between the two periods. Due to the changes in the spatial structure of the SAM, as well as those of the ENSO, SST variability in the SH displays a marked change between the two periods. Detailed descriptions of the decadal changes of the SH SST in terms of interaction in the oceanic and atmospheric variability are presented along with the possible implications of this change.

1 Introduction

The Southern Hemisphere (SH) high latitudes play an important role in the global climate system: the Southern Ocean acts as an important sink for heat and carbon dioxide; sea ice impacts the surface energy budget and is an important component for driving atmospheric circulation; and strong westerly winds over the Southern Ocean drive the strong current system, which is critical to global ocean circulation (Mayewski et al. 2009). The climate in the extra-tropical SH is dominated by two primary modes of variability: the high-latitude response to El Niño–Southern Oscillation (ENSO) (Harangozo 2000; Karoly 1989; Mo and Higgins 1998); and variations in the Southern Annular Mode (SAM) (Gong and Wang 1999; Thompson and Wallace 2000).

ENSO is the most prominent coupled mode involving atmospheric and oceanic variability over the tropical Pacific and exerts strong impacts on the climate over the extra-tropics through the excitation of a large-scale atmospheric wave train (Alexander et al. 2002; Trenberth et al. 1998). In the SH extra-tropics, a signature of a wave train associated with anomalous equatorial heating constitutes a series of alternating positive and negative geopotential height anomalies extending from the west central tropical Pacific toward the southeast Pacific near Antarctica–South America. This so-called Pacific–South America (PSA) pattern, which was first identified by Karoly (1989), is similar to its counterpart in the Northern Hemisphere, the Pacific–North America (PNA) pattern (Wallace and Gutzler 1981).

S.-R. Yeo · K.-Y. Kim (✉)
School of Earth and Environmental Sciences, Seoul National University, Seoul 151-742, Republic of Korea
e-mail: kwang56@gmail.com; kwang56@snu.ac.kr

S.-R. Yeo
CSIRO Marine and Atmospheric Research, Aspendale, VIC, Australia

The ENSO-induced atmospheric teleconnection, in turn, modulates Antarctic sea ice as well as sea surface temperature (SST) in the Southern Ocean through alteration of the surface energy fluxes (Ciasto and Thompson 2008; Ciasto and England 2011; Li 2000; Renwick 2002; Simpkins et al. 2012; Verdy et al. 2006; Yuan 2004).

Climate in the extra-tropical SH is also strongly influenced by the SAM, which is a dominant mode of the SH atmospheric circulation. The SAM is represented as the first empirical orthogonal function (EOF) mode of the monthly 500-hPa geopotential height (Rogers and van Loon 1982; Screen et al. 2010) and is characterized by a zonally symmetric pattern with pressure anomalies of opposite signs over the mid-latitudes and Antarctica. The positive phase of the SAM is associated with a positive atmospheric pressure anomaly in the mid-latitudes together with a negative anomaly in Antarctica and vice versa for the negative phase of the SAM. Previous studies have shown that the SAM has a profound impact on SH climate variability (e.g., Sen Gupta and England 2006; Lefebvre et al. 2004; Mo 2000; Screen et al. 2010; Stammerjohn et al. 2008). In particular, changes in surface westerly winds by the SAM directly affect Ekman flow as well as air–sea fluxes, which drive SH SST anomalies (Ciasto and Thompson 2008; Screen et al. 2010; Verdy et al. 2006). Although the variability associated with the SAM has a mostly zonal structure, as its name implies, the SAM also possesses a zonally asymmetric component in the pressure and wind pattern. This non-annular component of the SAM yields a clear local impact on the SH climate (Hall and Visbeck 2002; Lefebvre et al. 2004; Limpasuvan and Hartmann 2000). For example, locally enhanced low-pressure anomaly to the west of the Antarctic Peninsula during a positive SAM phase results in advection of warm air and subsequent warming in the Antarctic Peninsula.

Given the importance of ENSO and the SAM to the SH climate, there is a need to consider decadal variability of ENSO and the SAM and their signals in the SH climate. Yeo et al. (2012) demonstrated that the ENSO has experienced a significant decadal change around 1998–1999 in terms of its spatial SST anomaly (SSTA) pattern such that the leading mode of the tropical Pacific SSTA was characterized by conventional El Niño with the SSTA center located in the eastern Pacific (i.e., Eastern Pacific (EP) El Niño) during the period 1980–1998, whereas it was characterized by the SSTA centered in the equatorial central Pacific (i.e., Central Pacific (CP) El Niño; Kao and Yu 2009) during 1999–2010. Further, many previous studies have shown that CP El Niño has occurred more frequently than EP El Niño during the late 1990s and the 2000s (e.g., Kug et al. 2009; Lee and McPhaden 2010; Yeh et al. 2009). Because EP and CP El Niño have different impacts on the global climate (Ashok et al. 2007; Larkin and Harrison 2005; Mo 2010; Taschetto

and England 2009; Weng et al. 2011), it is expected that the ENSO-related teleconnection pattern before and after the late 1990s may each be distinctive. Indeed, Yeo et al. (2012) suggested that the ENSO-related North Pacific climate variability experienced remarkable changes since 1998–1999 in association with the changes in the dominant mode of the tropical Pacific SSTA from EP to CP El Niño. In addition, there is a growing body of evidence suggesting that physical conditions in the tropical and North Pacific have significantly changed around 1998–1999 (Bond et al. 2003; Minobe 2000, 2002; Peterson and Schwing 2003; Schwing and Moore 2000; Yeo and Kim 2014; Yeo et al. 2014). This change is closely related to a striking phase transition of the Pacific Decadal Oscillation (PDO) (Mantua et al. 1997), which affects the basic climate state of the Pacific since ~2000; such changes include accelerated trade winds (England et al. 2014), rapid sea-level rise in the western tropical Pacific (Merrifield et al. 2012), cooling of the eastern and central tropical Pacific (Kosaka and Xie 2013), and other associated climate trends (Trenberth and Fasullo 2013). It should be noted, however, that there are different opinions on the changeover time. Based on these previous studies, the first objective of the present study is to extend the focus on the decadal changes in the SH climate in association with ENSO before and after the late-1990s.

Together with the ENSO-related decadal changes of the SH climate, the SAM-related decadal changes of the SH climate is also investigated in the present study. Yuan and Yonekura (2011) revealed through spectral analysis that decadal variability of the SAM is a statistically robust phenomenon in the SH climate system. Of particular interest in the present study is the decadal change of the spatial structure in the SAM-related pressure field because the variation of the non-annular component of the SAM results in different local climatic impacts. Thus, the second objective of this study is to identify the decadal changes in the SH climate that occurred in the late 1990s in association with the changes in the spatial structure of the SAM.

Particular focus is placed on the ENSO- and the SAM-related SH SSTA and their physical processes by examining surface energy fluxes as well as atmospheric circulation. Analyses are conducted separately for the 20-year period of 1979–1998 and for the 14-year period of 1999–2012. No previous study has indicated decadal changes in the SAM structure in the late 1990s. As will be seen in Sect. 4, however, structural change of the SAM is obvious before and after the late 1990s. For convenience, the two periods are hereinafter referred to as the first and second periods, respectively. The major analysis tools in the present study are the cyclostationary empirical orthogonal function (CSEOF) method and regression analysis in CSEOF space. The details of the CSEOF and regression analyses are presented in Sect. 2 along with a description of the data used

in this study. The decadal changes of the ENSO-related SH climate are examined in Sect. 3, and those of the SAM-related SH climate are examined in Sect. 4. Section 5 provides the relevance of ENSO and the SAM in explaining the observed characteristics of SSTA in the SH high latitudes. A discussion and concluding remarks of this study are presented in the final section.

2 Data and methodology

Monthly mean oceanic and atmospheric datasets for the 34-year period from 1979 to 2012 were used in the present study. This period was chosen because it incorporates satellite measurements of near-continuous and globally comprehensive surface observations, allowing reliable analysis of the SH climate variability. The monthly mean SST data were obtained from the Extended Reconstruction SST version 3 (ERSST. v3) (Smith et al. 2008), which is available on a 2° longitude × 2° latitude resolution. The monthly mean atmospheric fields including geopotential height and zonal and meridional winds derived from the National Center for Environmental Prediction/Department of Energy (NCEP/DOE) reanalysis 2 dataset (Kanamitsu et al. 2002) at a horizontal resolution of 2.5° longitude × 2.5° latitude. The surface wind stress fields were also obtained from the NCEP/DOE dataset and have spatial coverage of a T62 Gaussian grid for driving Ekman heat fluxes. The monthly mean surface heat flux datasets, including latent and sensible heat, were obtained from the Objectively Analyzed Air–Sea Fluxes (OAFlux) (Yu and Weller 2007), which have been developed by the Woods Hole Oceanographic Institution.

The present study used CSEOF analysis (Kim and North 1997; Kim et al. 1996) to extract principal modes of SH climate variability. In this method, space–time data, $T(r, t)$, are decomposed into cyclostationary loading vectors, $LV_n(r, t)$, and their corresponding principal component time series, $PC_n(t)$, as

$$T(r,t) = \sum_n LV_n(r,t)PC_n(t), \qquad (1)$$

where n, r, and t denote the mode number, space, and time, respectively. The CSEOF method has a strong advantage in capturing spatial patterns that vary in time and space. This is possible because the CSEOF loading vectors are time dependent and periodic with the nested period, d, as

$$LV_n(r,t) = LV_n(r,t+d), \qquad (2)$$

The nested period represents the periodicity of statistics of a given dataset and is associated with the inherent time scales of the physical processes in the data. In this study, the nested period was set to 12 months because the

statistics of the climate datasets exhibit primarily one-year periodicity in accordance with the seasonal variation in insolation. Thus, the physical evolution for a 12-month period is described in each CSEOF loading vector, which is modulated over a longer time span by corresponding PC time series.

A regression analysis in CSEOF space was conducted to understand the physical relationship between a target variable and a predictor variable. Because the main purpose of the present study is to understand SH SST variability, SST was considered as the target variable, and other variables were the predictor variables. After CSEOF analysis was conducted on each predictor variable, the PC time series of the predictor variable, $PCP_m(t)$, was regressed onto the PC time series of the target variable, $PC_n(t)$, as

$$PC_n(t) = \sum_{m=1}^{M} \alpha_m^{(n)} PCP_m(t) + \varepsilon^{(n)}(t), \quad n = 1, 2, 3, \ldots, \quad (3)$$

where $\alpha_m^{(n)}$ and $\varepsilon^{(n)}(t)$ represent the regression coefficients and the regression error time series, respectively. In this study, 20 predictor time series were used for the regression analysis ($M = 20$). The degree of fitting for each mode was measured by the R^2 value, which is given by $1 - var[\varepsilon_n(t)]/var[PC_n(t)]$. The new loading vectors for the predictor variable, $LVPR_n(r, t)$, were obtained by using the regression coefficient as

$$LVPR_n(r,t) = \sum_{m=1}^{M} \alpha_m^{(n)} LVP_m(r,t), \qquad (4)$$

where $LVP_m(r, t)$ are the CSEOF loading vectors for the predictor variable. As a result of regression analysis in CSEOF space, regressed spatial patterns of the predictor variables become physically and dynamically consistent with the target patterns by sharing identical amplitude time series.

3 Decadal changes of ENSO-related SH climate variability

The dominant modes of SST variability over the SH high-latitude during the two sub-periods (1979–1998 and 1999–2012) were calculated through CSEOF analysis. Figures 1 and 2 illustrate the first two CSEOF modes of SSTA over the SH high-latitude (60°–80°S) and their corresponding PC time series (black curves), along with the regressed SSTA over the SH mid-latitude (30°–60°S) for the period of 1979–1998 (left panels of Figs. 1, 2) and the period of 1999–2012 (right panels of Figs. 1, 2), respectively. Because the monthly spatial patterns do not change significantly, seasonal (3-month) mean SSTA patterns are
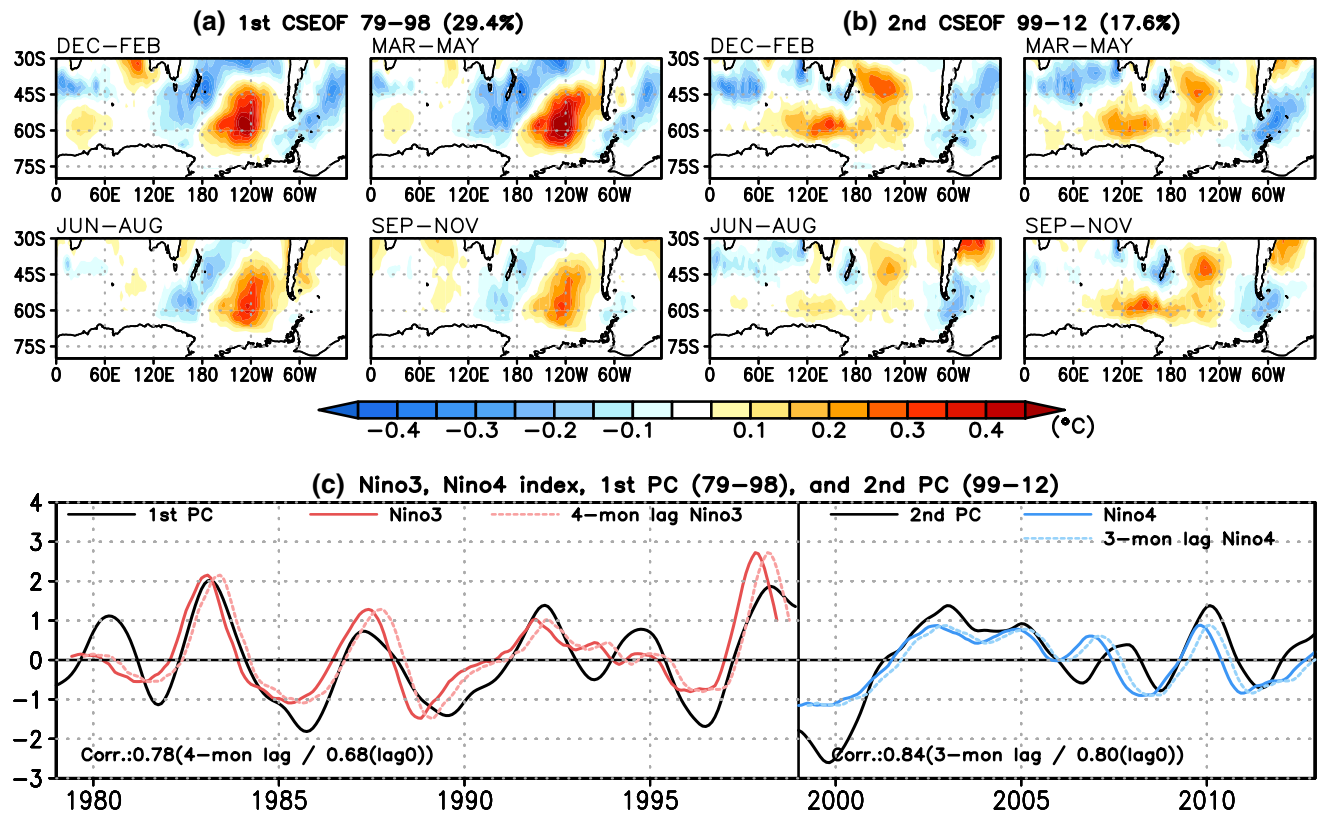
Fig. 1 a The first cyclostationary empirical orthogonal function (CSEOF) loading vector of the Southern Hemisphere (SH) high-latitude (60°–80°S) sea surface temperature anomaly (SSTA) for the period 1979–1998. The SH mid-latitude (30°–60°S) region depicts the regression of the SSTA onto the first CSEOF loading vector in the SH high latitudes. **b** Same map as in (**a**) but for the second CSEOF mode for the period 1999–2012. Each panel represents the seasonal mean spatial pattern. *Black curves* in (**c**) show the principal component (PC) time series of the first CSEOF mode for the period 1979–1998 and the second CSEOF mode for the period 1999–2012. *Red* and *blue curves* in (**c**) represent 12-month moving averaged monthly Niño 3 index and Niño 4 index, respectively. All PC time series and the Niño indices are normalized

presented in the figures. The regressed mid-latitude SSTA patterns have R^2 values of more than 0.99 for the first and second modes during both periods, indicating that the regression fit is nearly perfect. In fact, the mid-latitude SSTA patterns matched seamlessly with the high-latitude SSTA patterns across the boundary (60°S). It should be noted that Fig. 1 (Fig. 2) consists of the first (second) mode for the period 1979–1998 and second (first) mode for the period 1999–2012; this grouping was based on the physics they represent, as is discussed subsequently.

3.1 ENSO-related SH SST variability

Figure 1a depicts the first CSEOF mode for the first period, and Fig. 1b depicts the second CSEOF mode for the second period, which explains approximately 29 and 17 % of the respective total variance. The corresponding PC time series (black curves in Fig. 1c) were strongly correlated with the Niño SST indices, indicating that these modes are closely related to tropical Pacific ENSO variability.

Correlation was 0.68 between the first PC time series for the first period and the 12-month moving averaged Niño 3 index, in which the SSTA was averaged over 90°–150°W, 5°S–5°N, as shown by the red curve in Fig. 1c; correlation exceeds a 95 % confidence level based on a two-tailed test of the *t* statistics. Moreover, the maximum correlation of 0.78 appeared when the PC time series was lagged by four months, as shown by the red dashed curve in Fig. 1c (see also Table 1). The second PC time series for the second period was also closely correlated with the Niño 3 index; the maximum correlation was 0.78 when the PC time series was lagged by 6 months (Table 1). It was found, however, that the second PC time series was more highly correlated with the Niño 4 index, in which the SSTA was averaged over 160°E–150°W, 5°S–5°N, as shown by the blue curve in Fig. 1c, with a simultaneous correlation of 0.80 and a maximum correlation of 0.84 when lagged by three months. As summarized in Table 1, the PC time series for the first period was more closely correlated with the Niño 3 index than the Niño 4 index, whereas that for the second
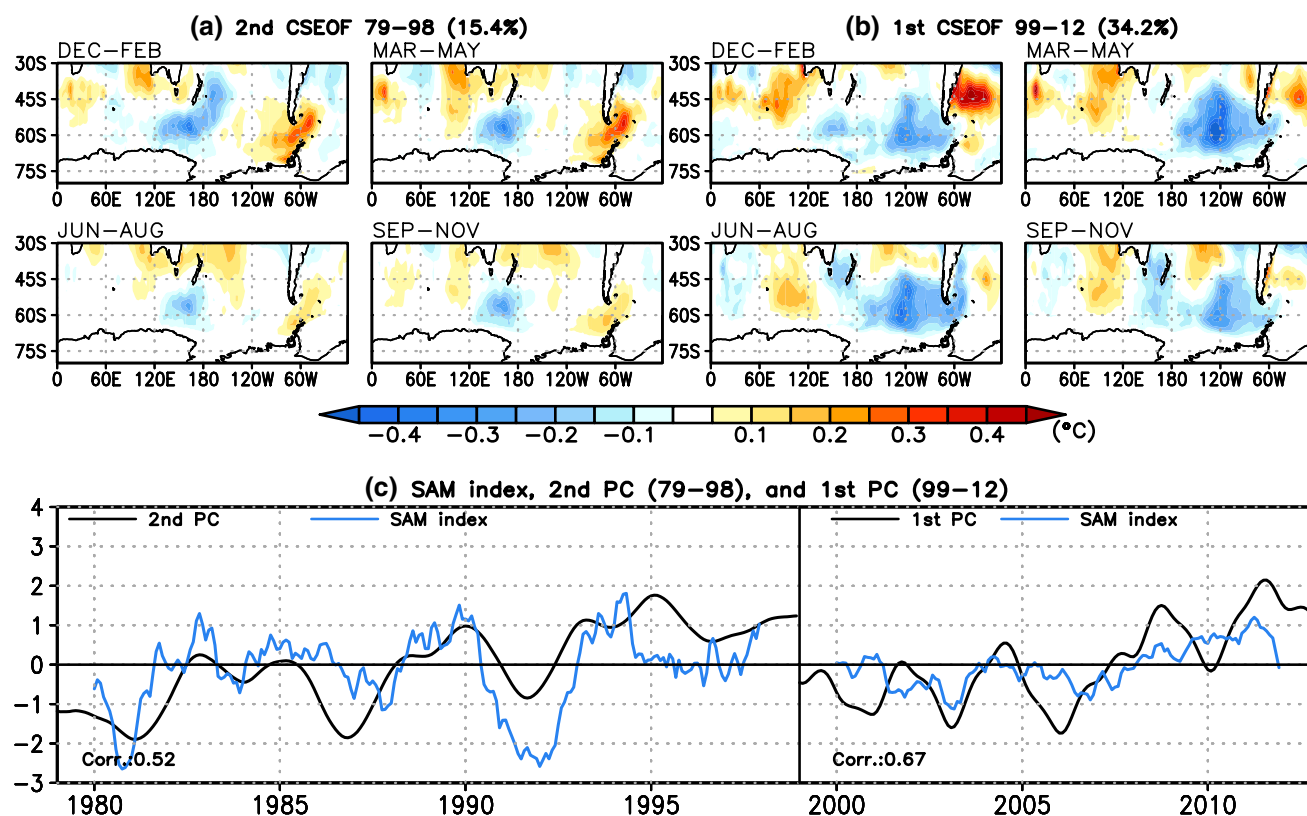
Fig. 2 The same map as in Fig. 1 but (**a**) for the second CSEOF mode for the period 1979–1998 and **b** the first CSEOF mode for the period 1999–2012. Black curves in (**c**) show the PC time series of the second CSEOF mode for the period 1979–1998 and the first CSEOF mode for the period 1999–2012. Blue curves in (**c**) represent 24-month moving averaged Southern Annular Mode (SAM) indices for both periods. All PC time series and the SAM indices are normalized

Table 1 Correlation coefficients between the two principal component (PC) time series of the Southern Hemisphere (SH) sea surface temperature (SST) and the Niño 3, Niño 4, and SAM indices

	PC1 for 1979–1998	PC2 for 1999–2012
Niño 3	0.68 (0.78 at lag 4)	0.67 (0.78 at lag 6)
Niño 4	0.59 (0.71 at lag 4)	0.80 (0.84 at lag 3)
	PC2 for 1979–1998	PC1 for 1999–2012
SAM	0.52	0.67

Left (right) column corresponds to the PC time series during the period 1979–1998 (1999-2012). Correlation coefficients are statistically significant at a 95 % level as determined by the two-tailed *t* test

period was more closely correlated with the Niño 4 index. This result suggests that the relationship between ENSO and the SH SST is somewhat different for the first and second periods such that the eastern tropical Pacific SSTA was instrumental for the ENSO–SH SST relationship during the first period and the central tropical Pacific SSTA was more involved during the second period.

A comparison between Fig. 1a, b reveals that the spatial structures of the ENSO-related SSTA differed significantly between the two periods. For the first period, the spatial

patterns were characterized by a broad region of positive SSTA over the South Pacific sector around 40°–70°S and 90°–170°W, negative anomalies centered around New Zealand stretching from Australia to South America along 30°–40°S, and other significant negative anomalies extending northeastward from the Drake Passage to the South Atlantic Ocean (Fig. 1a). This spatial pattern of SSTA was particularly evident during the austral summer (December–February) and was generally persistent throughout the year except during the austral winter (June–August); the negative SSTA over the Drake Passage and Atlantic Ocean was obscure during the austral winter. The SSTA structures presented in Fig. 1a are consistent with those in earlier studies investigating the SH SSTA in connection with primarily the conventional eastern Pacific El Niño (e.g., Garreaud and Battisti 1999; Holland et al. 2005; Kidson and Renwick 2002; Li 2000; Renwick 2002; Verdy et al. 2006).

For the second period, however, the SSTA patterns (Fig. 1b) were distinctive from those of the first period. The SH SSTA featured primarily a dipole structure around Antarctica with positive anomalies along 90°E–120°W and negative anomalies along 20°–90°W. This pair of SSTA around Antarctica extended northeastward and yielded a

Fig. 3 a The first CSEOF loading vector of the SH high-latitude SSTA (*shading*) during the period 1979–1998. The 850-hPa geopotential height anomaly (*contour*) and SSTA over the SH mid-latitude and the tropical Pacific (*shading*) were obtained from a regression analysis onto the first CSEOF loading vector of the SH high-latitude SSTA. Each panel shows the seasonal mean spatial pattern obtained by averaging over September–November (SON), December–February (DJF), March–May (MAM), and June–August (JJA). **b** The same map as in (**a**) but for the second CSEOF mode for the period 1999–2012
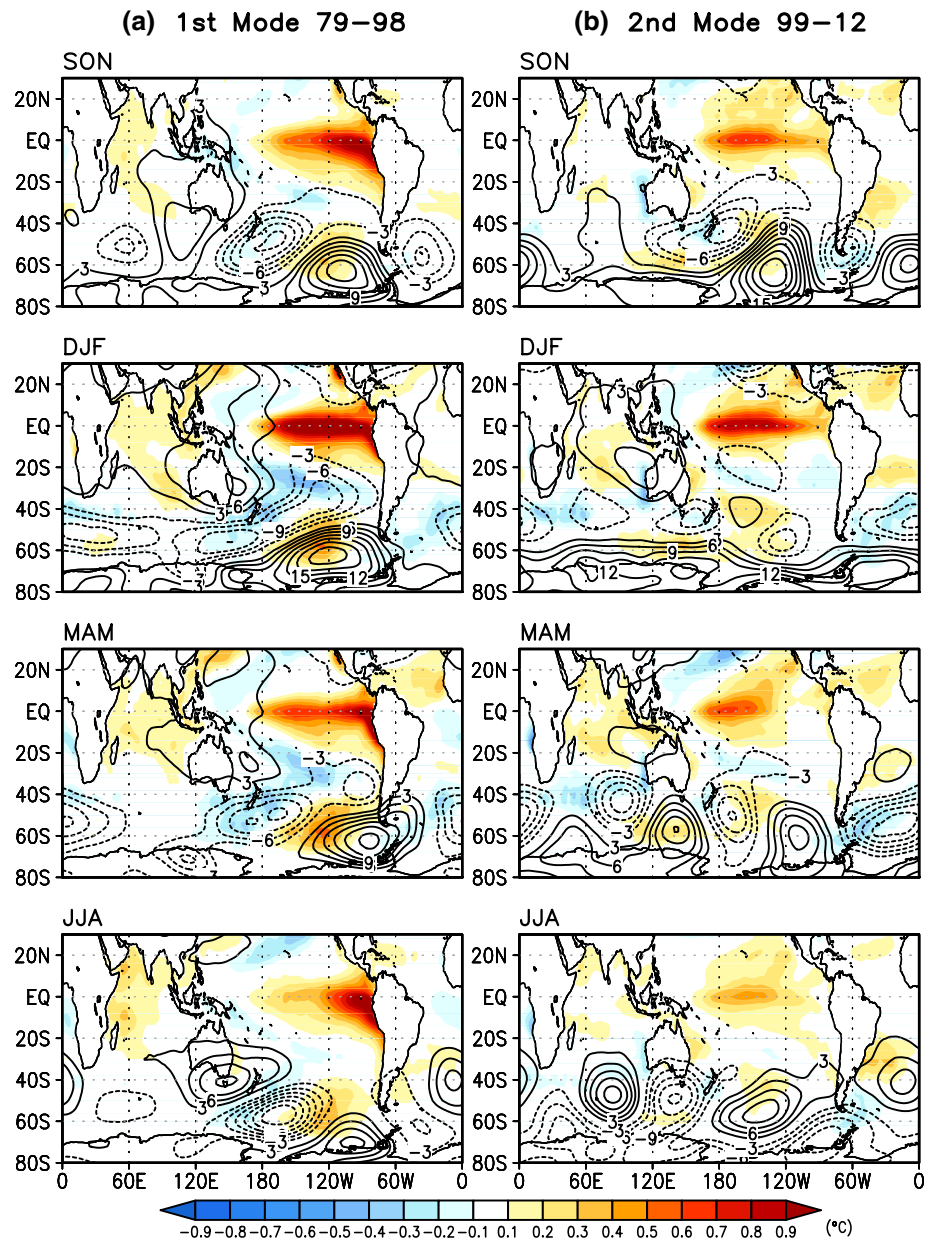
considerable area of positive SSTA to the east of New Zealand and a negative SSTA over the South Atlantic Ocean. The most notable difference of the ENSO-related SSTA between the two periods is the location of the positive SSTA over the Pacific; strong positive anomalies were centered on the Ross Sea in the first period, whereas positive anomalies only approximately half as strong were generally located over the Eastern Hemisphere in the second period.

3.2 ENSO-related SH atmospheric variability

To examine the detailed physical features of the ENSO-related SH climate variability for the two periods, regression analysis was conducted on the atmospheric and oceanic variables over the tropics and the SH (80°S–30°N). Figure 3 displays the regressed seasonal mean patterns of the SSTA and the 850-hPa geopotential height anomaly for the first period (left panels) and second period (right panels). Given an equivalent barotropic nature of variability in the high southern latitudes, the 850-hPa geopotential height anomaly can be regarded as a representative atmospheric circulation structure (Karoly 1989; Thompson and Wallace 2000). The R^2 values were more than 0.97 for SSTA and more than 0.99 for 850-hPa geopotential height for both periods. As illustrated in Fig. 3a, the SSTA patterns over the tropical Pacific depicted a characteristic EP El Niño signal with a positive anomaly centered on the equatorial eastern Pacific. It should be noted that the first PC time

series for the first period had a strong correlation with the Niño 3 index (Table 1). During the austral spring (September–November; first row of Fig. 3a), when the warm SSTA had begun to develop in the tropical Pacific, the Southern Ocean had not yet fully responded. The corresponding 850-hPa geopotential height anomaly exhibited a wave-like structure over the Southern Ocean with a dominant high-pressure anomaly over the Amundsen/Bellingshausen Seas. This feature is consistent with earlier studies in that a blocking high is quickly established in the southeastern Pacific when El Niño develops (Renwick and Revell 1999). During the austral summer (December–February; second row of Fig. 3a), when the El Niño magnitude was the strongest, the extra-tropical ENSO signal exhibited a classic horseshoe pattern with negative SSTA surrounding the equatorial warm anomaly. In the Southern Ocean, a negative anomaly, as a southern portion of the horseshoe pattern, prevailed over the subtropical south Pacific, whereas a positive anomaly prevailed over the southeastern Pacific around the Ross Sea region. This SSTA feature is physically consistent with the corresponding atmospheric circulation. The spatial structure of the 850-hPa geopotential height anomaly in the low-latitudes is characterized by an increase over the equatorial western Pacific and Australia, which is associated with suppressed convection during an El Niño event. In the mid- and high-latitudes, a series of geopotential height anomalies with alternating signs portray clear evidence of a wave train extending from the low-latitudes toward the southeastern Pacific. This wave train constitutes the so-called PSA pattern (Mo and Higgins 1998), which is considered as the Rossby wave response to the anomalous equatorial heating (Karoly 1989). Dynamical consistency between the atmospheric circulation and SSTA fields is clear: the northwestern flank of the strong anticyclonic (cyclonic) anomaly over the southeastern (southwestern) Pacific is associated with warm (cold) air advection by the northerly (southerly) flow, which tends to increase (decrease) SST. In the following two seasons, the high- and low-pressure centers over the SH were weakened, and the associated SSTA was also weakened in conjunction with the attenuation of the El Niño SSTA. Nonetheless, the overall circulation structure did not significantly change during the entire season in terms of the wave train pattern extending poleward from the subtropics west of the dateline to the South Pacific and South America.

We then investigated the ENSO-related SH atmospheric and oceanic variability during the second period (1999–2012). As suggested by the high correlation between the second PC time series and the Niño 4 index (Table 1), the SSTA pattern presented in Fig. 3b shows the strongest warming signal in the equatorial central Pacific, which closely resembles the characteristic feature of CP El Niño. This result is consistent with earlier studies that suggest

that CP El Niño has occurred more frequently than EP El Niño during the late 1990s and the 2000s (e.g., Kug et al. 2009; Lee and McPhaden 2010; Yeh et al. 2009). The ENSO-related SH atmospheric and oceanic variability for the second period differed significantly from that of the first period, corresponding with previous reports that state these two types of El Niño have different impacts on the global climate (Ashok et al. 2007; Larkin and Harrison 2005; Mo 2010; Weng et al. 2011).

A comparison between Fig. 3a, b reveals several remarkable differences between the two periods in terms of the SSTA and atmospheric circulation fields. During the austral spring season, the tropical Pacific warm SSTA center was located in the eastern Pacific and was attached to South America in the first period. In contrast, the tropical Pacific warming center for the second period was located in the central Pacific, which further extended toward the northeastern Pacific. The corresponding SH atmospheric circulation pattern was also notably distinctive from that of the first period. In particular, a high-pressure anomaly in the South Pacific extended over the eastern Pacific region (Amundsen/Bellingshausen Seas) for the first period and the central Pacific (120°–140°W) for the second period. It should be noted that the two low-pressure anomalies were located over the Weddell Sea and near the dateline for the first period, whereas they were located over the Drake Passage and near New Zealand for the second period. Overall, the spatial structure of the SH atmospheric circulation for the second period was characterized by a ~20° westward shift of the active centers compared with the first period. The accompanying SSTA for the second period exhibited warming over the southern central Pacific region, in which the northerly wind anomaly advected warm air along the northwestern flank of the high-pressure anomaly to produce oceanic warming. These differences in ENSO-related atmospheric and oceanic variability between the two periods appear to be primarily due to the different types of ENSO for the two periods. The two types of El Niño generate different structures of Rossby wave train in association with the convective forcing over the tropical Pacific. As suggested in earlier studies (Harangozo 2004; Lachlan-Cope and Connolley 2006), the position of the convection in the tropical Pacific is an important factor in the downstream response during an El Niño event. It should be noted that the high-pressure anomaly over the subtropical western Pacific, which is related to the suppressed convection during El Niño, was evident in the first period, but such a structure was obscure in the second period, implying that the Rossby wave response was weaker in the second period. Such a difference also appeared during the austral summer (December–February), when the high-latitude atmospheric circulation pattern exhibits strong zonal symmetry in contrast to the wavelike structure in the first period. In the

following two seasons, the atmospheric circulation pattern was characterized by a wavenumber-3 pattern, which does not appear to be directly linked to the Rossby wave train from the tropical Pacific.

3.3 ENSO-related heat flux variability

Many studies have suggested that ENSO-driven large-scale atmospheric teleconnection impacts extratropical SST variability through alteration of the surface energy fluxes and horizontal oceanic heat transport by Ekman currents (Alexander et al. 2002; Ciasto and Thompson 2008; Ciasto and England 2011; Frankignoul 1985; Verdy et al. 2006) in addition to the thermal advection in the atmosphere. Over the SH extra-tropics in particular, the ENSO-related SST changes are induced by surface turbulent heat flux, which is the sum of latent heat and sensible heat fluxes, and heat flux resulting from anomalous Ekman advection in the upper ocean, hereinafter referred to as the Ekman heat flux (Ciasto and Thompson 2008; Ciasto and England 2011). The Ekman heat flux can be calculated by using horizontal wind stress and the SST gradient as

$$F_{EK} = \frac{C_p}{f}\left(-\tau_y\frac{\partial T}{\partial x} + \tau_x\frac{\partial T}{\partial y}\right), \tag{5}$$

where C_p is the heat capacity of seawater; f is the Coriolis parameter; τ_x and τ_y are the zonal and meridional wind stresses, respectively; and $\partial T/\partial x$ and $\partial T/\partial y$ are the zonal and meridional gradients of SST, respectively.

In order to understand the detailed physical processes of the ENSO-related SST variability for the two periods, the ENSO-related turbulent and Ekman heat fluxes were investigated and compared with the patterns of SSTA. Figure 4 shows the austral spring (September–November) regressed patterns of the turbulent (top row) and Ekman (middle row) heat flux anomalies along with the 850-hPa wind anomaly (vector) for the first (left panel) and second (right panel) periods; the R^2 values for all of the variables were more than 0.97. The bottom panels in Fig. 4 show the SSTA reproduced from Fig. 3. We focused on the austral spring when the tropical–extratropical connection is enhanced (Jin and Kirtman 2009). Positive (negative) turbulent heat flux denotes a flux from the atmosphere (ocean) to the ocean (atmosphere), whereas positive (negative) Ekman heat flux indicates warm (cold) water advection driven by poleward (equatorward) Ekman transport induced by anomalous easterlies (westerlies).

The pattern of turbulent heat flux anomalies for the first period is consistent with the overlying atmospheric flows, particularly over the South Pacific. For example, the region of positive turbulent heat flux anomaly (i.e., from the atmosphere to the ocean) over the southeastern Pacific coincides with the easterly wind anomaly, which indicates

a significant decrease of the climatological westerly flow leading to anomalous downward heat flux. In addition, a significant positive turbulent heat flux anomaly to the south of Australia appears to be related to the overlying anticyclonic circulation anomaly (Fig. 3a). Moreover, the pattern of Ekman heat flux anomaly shown in the middle panel of Fig. 4a is in line with the horizontal wind anomaly such that the easterly wind anomaly over the southeastern Pacific results in a poleward transport of relatively warm water, leading to a positive Ekman heat flux anomaly whereas the westerly wind anomaly over the southwestern Pacific causes an equatorward transport of relatively cold water leading to a negative Ekman heat flux anomaly. A comparison between the patterns of Ekman heat flux anomaly and SSTA reveals that the anomalous Ekman heat flux plays a significant role in the generation of ENSO-related SSTA, primarily in the Pacific sector. The anomalous turbulent heat flux, to a lesser extent, contributes to the SSTA.

The patterns of turbulent and Ekman heat flux anomalies for the second period are shown in Fig. 4b. In the second period, the wind anomaly over the South Pacific sector exhibited an enhanced meridional wind component compared with the first period. The turbulent heat flux anomaly was generally consistent with the meridional wind anomaly. That is, the southerly wind anomaly advected cold air, leading to an upward turbulent heat flux anomaly, whereas the northerly wind anomaly advected warm air, leading to a downward turbulent heat flux anomaly (top panel in Fig. 4b). It is noteworthy that the anomalous patterns of turbulent heat flux for the two periods differed appreciably, although the geopotential height anomaly fields for the two periods shared some degree of similarity (Fig. 3). The Ekman heat flux anomaly (middle panel in Fig. 4b), however, followed the zonal wind anomaly, and its amplitude was stronger than the turbulent heat flux anomaly. Thus, the Ekman heat flux appears to have a greater impact on the SSTA compared with the turbulent heat flux. It should be noted that the eminent features in the anomalous Ekman heat flux over the South Pacific were evident in the corresponding SSTA pattern (bottom panel in Fig. 4b). For example, a positive SSTA extending from the south central Pacific to the southwestern Pacific was consistent with the positive Ekman heat flux anomaly in that region, and the negative Ekman heat flux anomaly around New Zealand was also mirrored in the SSTA field. However, the similarity between the turbulent heat flux anomaly and SSTA was weak except over the South Atlantic Ocean and in the vicinity of the Drake Passage. Moreover, the correspondence between the turbulent and Ekman heat flux anomalies and the SSTA were less evident outside of the South Pacific sector for both periods; the lack of a strong link may be related to the fact that the ENSO-related SSTA was dominant over the South Pacific sector.
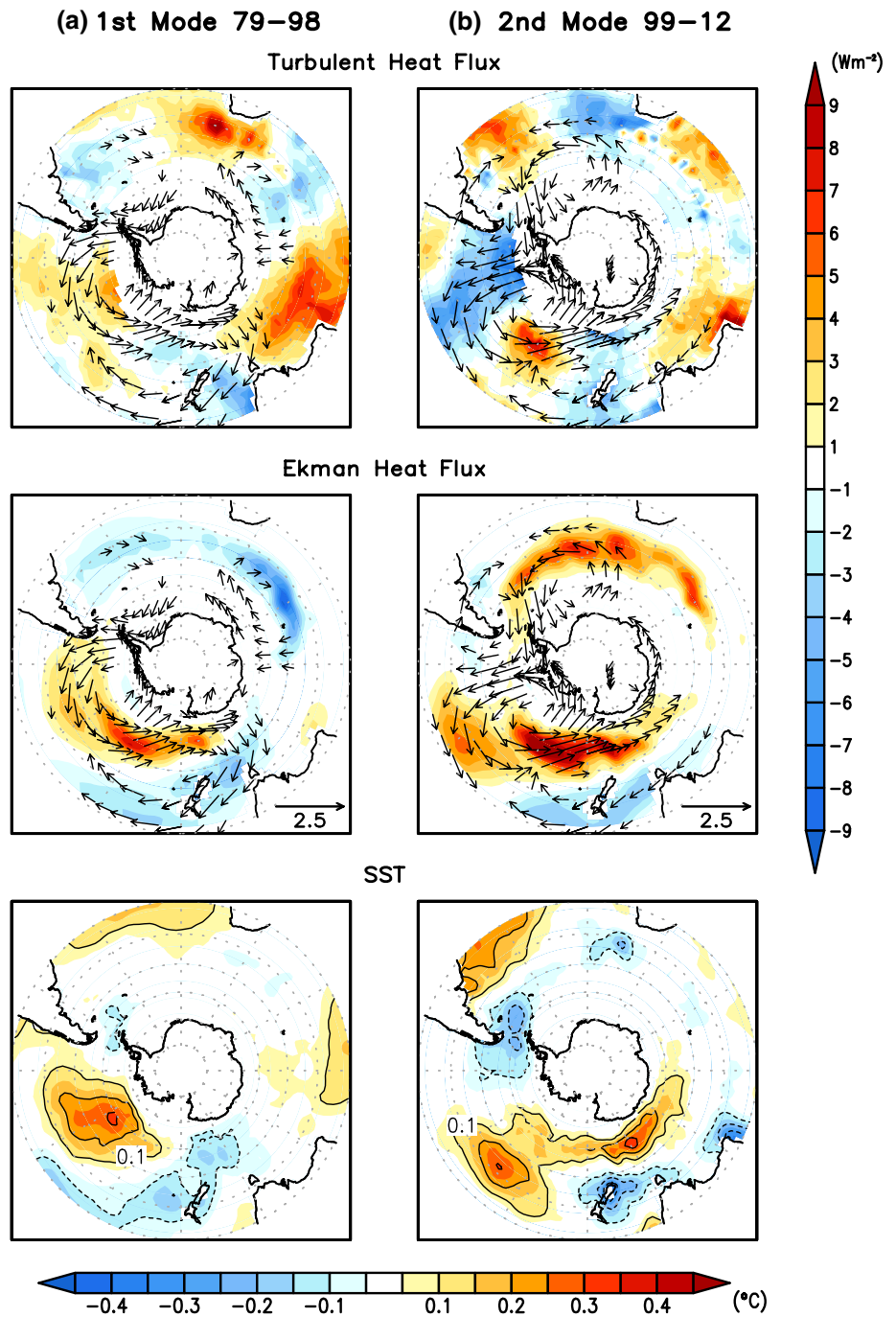
4 Decadal changes of the SAM-related SH climate variability

4.1 SAM-related SH SST variability

A major component of atmospheric variability in the SH is the SAM, representing a zonally symmetric exchange of mass between mid- and high- southern latitudes (Gong and Wang 1999; Thompson and Wallace 2000). Given the importance of the SAM to the SH climate, we next

examined the climate variability associated with the decadal change of the SAM. Figure 2a, b display the second CSEOF mode for the first period (1979–1998) and the first CSEOF mode for the second period (1999–2012), which explains approximately 15 and 34 % of the total variance in the dataset for the first and second period, respectively. The corresponding PC time series for both periods (black curves in Fig. 2c) and the SAM index, which is defined as the leading EOF PC time series of monthly 500-hPa geopotential height anomalies poleward of 20°S, shared some

degree of similarity. Correlation between the PC time series and the 24-month moving averaged SAM index (blue curve in Fig. 2c) was 0.52 for the first period and 0.67 for the second period, which is significant at a 95 % confidence level, reflecting that these two modes are closely related to the SAM variability, particularly on low-frequency time scales (Table 1). Previous studies reported that the SAM variability is related to the ENSO variability (e.g., L'Heureux and Thompson 2006). It should be noted, however, that the SAM-related modes shown in Fig. 2 are nearly independent of the ENSO-related modes shown in Fig. 1. Further, regression patterns based on the SAM index after removing the ENSO variability result in spatial patterns that are similar to Fig. 2.

Although these two modes both are correlated with the SAM index, the spatial structures of the SAM-related SSTAs for the two periods shown in Fig. 2a, b differed significantly. In the first period, the SAM-related SSTA patterns were characterized by a dipole structure with a positive anomaly over the Bellingshausen Sea and the Drake Passage and a negative anomaly over the western Pacific (120°E–180°) (Fig. 2a). The spatial structure of the SAM-related SSTA for the second period, presented in Fig. 2b, exhibited predominant cooling over much of the southeastern Pacific and warming over the Atlantic and Indian Oceans at latitudes of 35°–50°S. The amplitude of the SAM-related SSTA was largest during the austral summer (December–February) for both periods. These notable differences in the SAM-related SSTA between the two periods may be attributed to the decadal change of the SAM variability in the late 1990s.

4.2 SAM-related SH atmospheric variability

In order to identify the different characteristic features of the SAM between the two periods, the 500-hPa geopotential height anomalies were regressed onto the SAM-related SST variability, and the resulting spatial patterns are presented in Fig. 5. In the figure, seasonal-mean spatial patterns of SSTA (shading) and 500-hPa geopotential height anomalies (contour) for the austral warm (November–April; top panel) and cold (May–October; bottom panel) seasons are presented. The left (right) panel corresponds to the first (second) period. As evidenced by significant correlation between the PC time series and the SAM index presented in Fig. 2c, the regressed patterns of 500-hPa geopotential height anomalies reasonably captured the general structure of the SAM with lower than normal height over the polar region and higher than normal height over the SH mid-latitudes for both periods (Fig. 5). This atmospheric structure was more evident during the warm season and is largely comparable at all levels of the troposphere, i.e., barotropic.

Although the atmospheric circulation patterns for both periods possessed the characteristic feature of the SAM, they also have a significant non-annular component, as expressed by locally enhanced pressure anomalies. Indeed, earlier studies have reported that the SAM displays appreciable zonal asymmetry, yielding a significant meridional component of surface wind stress, which has a clear local impact on SST as well as atmospheric temperatures (Hall and Visbeck 2002; Lefebvre and Goosse 2005; Lefebvre et al. 2004; Limpasuvan and Hartmann 2000; Screen et al. 2009; Stammerjohn et al. 2008).

During the warm season of the first period (Fig. 5a), the regressed geopotential height anomaly displayed zonal asymmetry over the Drake Passage in the form of a ridge. Two centers of positive anomalies were also apparent in the mid-latitudes (30 and 120°E). Because of this asymmetry, surface wind stress has a significant meridional component, which affects local SSTA. For example, the northerly flows tended to increase SST over the northwestern part of the two high-pressure anomalies. Moreover, the decreased westerly over the Bellingshausen Sea and the Drake Passage resulted in warming of the ocean mixed layer by reducing the heat flux from the surface of the ocean, whereas the opposite situation prevailed over the western Pacific where the increased westerly induced a cold SSTA.
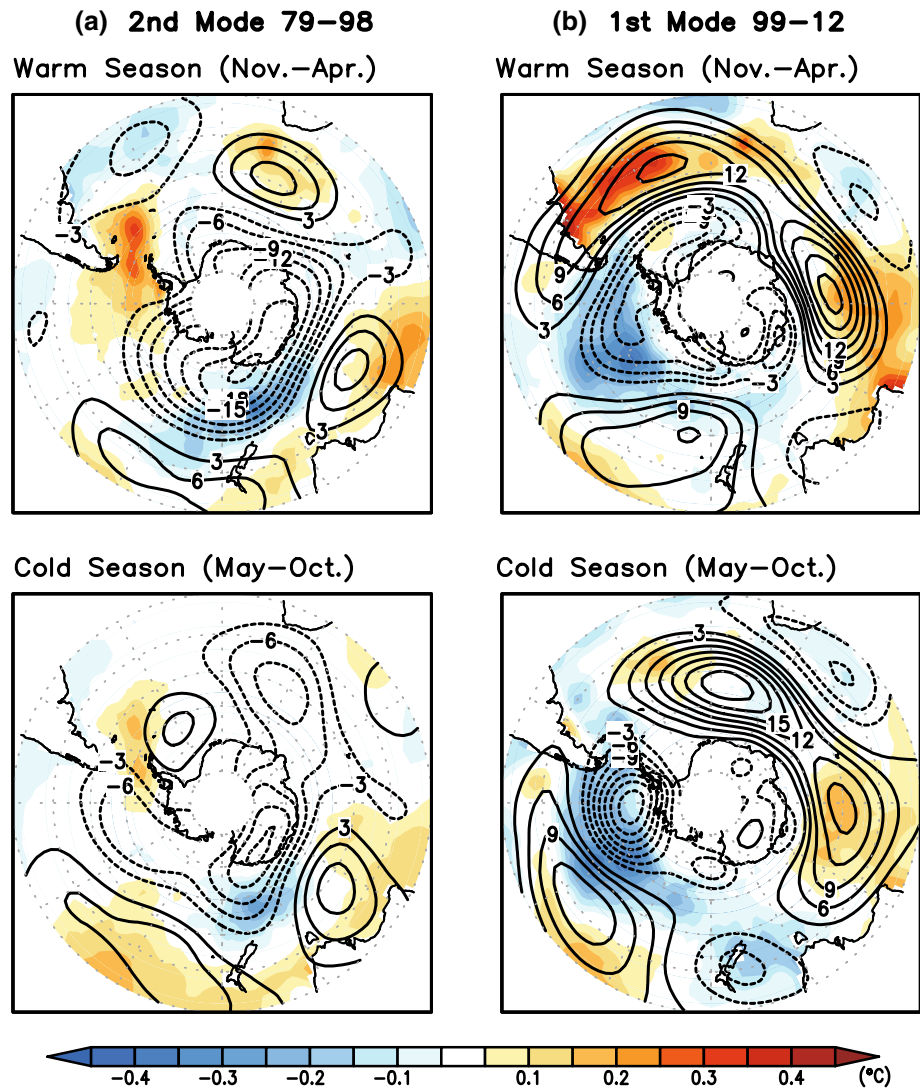
During the warm season of the second period (Fig. 5b), however, the regressed geopotential height anomalies displayed zonal asymmetry in the eastern central Pacific sector (90°–140°W), forming a trough around 110°W. As a result, the increased wind speed and cold air advection by the northward flow induced cooling in the central Pacific. Thus, the large regional differences in the SSTA patterns between the two periods may be attributed to the zonally asymmetric component of the SAM structure.

4.3 SAM-related heat flux variability

To further examine the detailed physical processes of the SAM-related SST variability for the two periods, turbulent and Ekman heat fluxes were investigated through regression analysis in CSEOF space. Figure 6 is analogous to Fig. 4 but shows patterns regressed onto the SAM-related modes (i.e., the second mode for the first period and the first mode for the second period). Focus was placed on the austral warm season (November–April) because the SAM-related atmospheric and oceanic variability is more evident in the warm season than in the cold season (Fig. 5).

The turbulent heat flux anomalies for the first period (top panel in Fig. 6a) exhibited generally negative values such as upward heat flux except over the high-pressure anomaly regions of 30°E, 120°E, and 160°W. Moreover, the Ekman heat flux anomalies (middle panel in Fig. 6a) displayed a zonally elongated negative anomaly stretching over

Fig. 5 **a** The second CSEOF loading vector of the SH high-latitude SSTA (*shading*) during the period 1979–1998. The 500-hPa geopotential height anomaly (*contour*) and SSTA over the SH mid-latitudes (*shading*) were obtained from a regression analysis onto the first CSEOF loading vector of the SH high-latitude SSTA. Each *panel* shows the seasonal mean spatial pattern by averaging over the austral warm season (November–April) and cold season (May–October). **b** The same map as in (**a**) but for the first CSEOF mode for the period 1999–2012

(a) 2nd Mode 79–98
Warm Season (Nov.–Apr.)

(b) 1st Mode 99–12
Warm Season (Nov.–Apr.)

Cold Season (May–Oct.)

Cold Season (May–Oct.)

−0.4   −0.3   −0.2   −0.1   0.1   0.2   0.3   0.4   (°C)

much of the circumpolar region of 50°–60°S, and positive anomalies were found north of 30°–40°S. This structure is apparent from the horizontal wind anomalies; a westerly (easterly) anomaly leads to a negative (positive) heat flux anomaly from the definition of the Ekman heat flux. A comparison shows that the resemblance between the turbulent heat flux and SSTA patterns appears to be weaker than that between the Ekman heat flux and SSTA patterns. Specifically, the cold SSTA over the western Pacific and the warm SSTA south of Australia and Africa are fairly consistent with the Ekman heat flux anomalies. Over the Drake Passage, however, both the turbulent and Ekman heat flux anomalies did not project onto the warm SSTA pattern. The reason for this discrepancy is not clear, although it appears that heat flux anomalies alone cannot fully explain the SAM-related SSTA.

The regressed patterns of turbulent and Ekman heat flux anomalies for the second period are presented in Fig. 6b. In

the second period, the main features of the Ekman heat flux anomalies (middle panel in Fig. 6b) were well mirrored in the SSTA pattern and included both the negative anomalies in the central Pacific and the positive anomalies stretching over the mid-latitude Indian and Atlantic Oceans. The turbulent heat flux anomalies (top panel in Fig. 6b) displayed a tri-pole structure in the Pacific sector, which also exerted influence on the Pacific SSTA. The Ekman heat flux appears to be more efficient than the turbulent heat flux in driving the SAM-related SSTA.

5 Decadal changes of the SH SST in association with the ENSO and the SAM

Having identified the decadal changes of SH SST variability in connection with ENSO and the SAM, we then assessed how a large degree of the observed SST variability

Fig. 6 The same map as in Fig. 4 but for the seasonal mean spatial pattern of the Austral warm season (November–April) **a** for the second CSEOF mode for the period 1979–1998 and **b** the first CSEOF mode for the period 1999–2012

(a) 2nd Mode 79−98 **(b) 1st Mode 99−12**

Turbulent Heat Flux

Ekman Heat Flux

SST
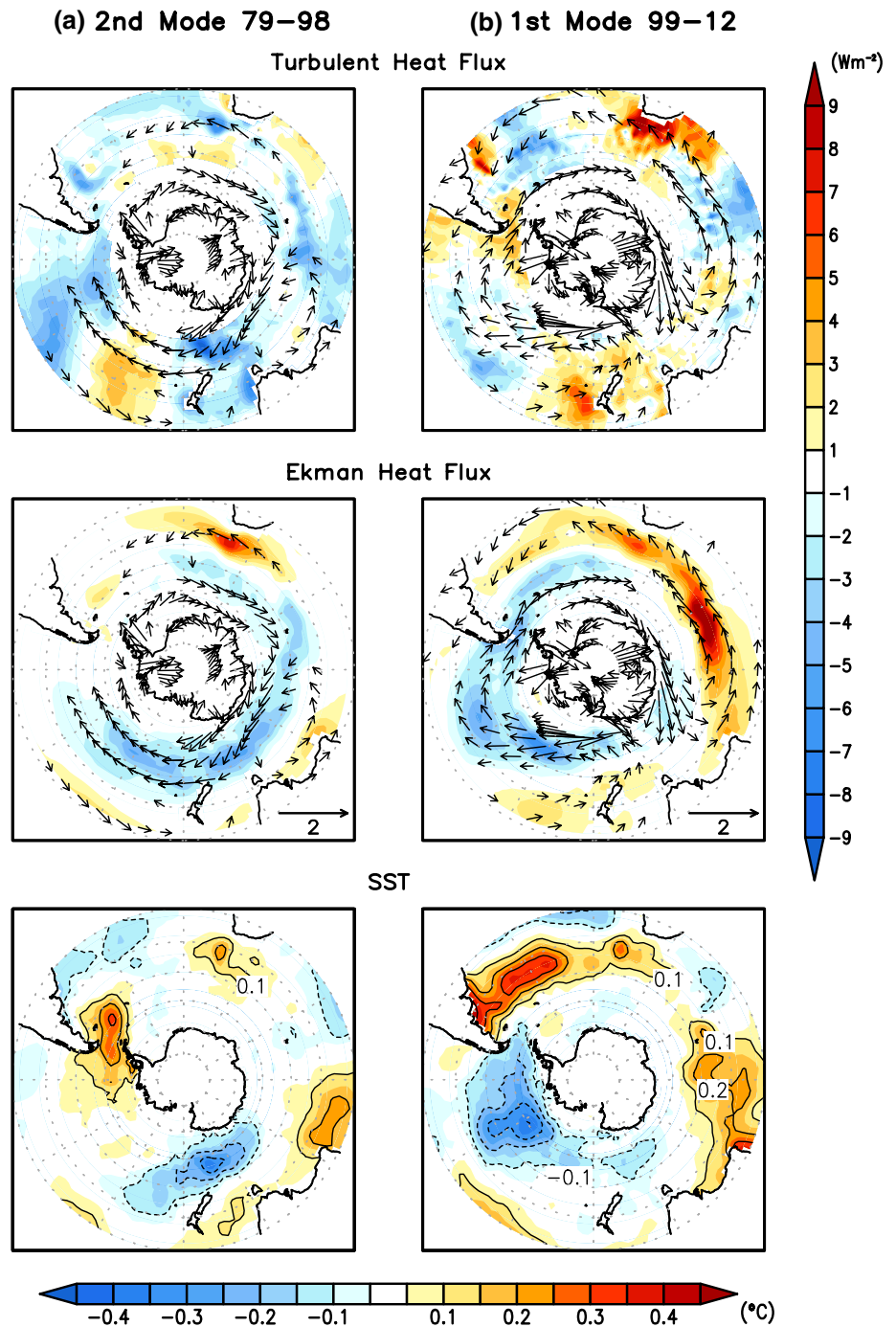
in the Southern Ocean can be explained by these two modes. The spatio-temporal evolution characteristics of SST variability associated with each CSEOF mode can be easily understood by reconstructing SSTA using the particular mode. Reconstruction of SSTA was accomplished by multiplying the loading vector with the corresponding PC time series for a particular CSEOF mode; it should be noted that the loading vector was periodic. Figure 7a, b display the longitude–time plot of the reconstructed SSTA averaged over 60°–70°S associated with the ENSO and the

SAM, respectively; the ENSO (SAM)-related SSTA reconstruction consisted of the first (second) CSEOF mode for the period of 1979–1998 and of the second (first) CSEOF mode for the period of 1999–2012. As revealed in the previous section, Fig. 7a, b highlight the remarkable changes in both the ENSO- and the SAM-related SST structures over the SH high latitudes before and after 1998–1999. In the first period, the ENSO-related high-latitude SST variability exhibited a tri-pole structure in the Pacific sector with a primary active center in the Ross Sea. In the second
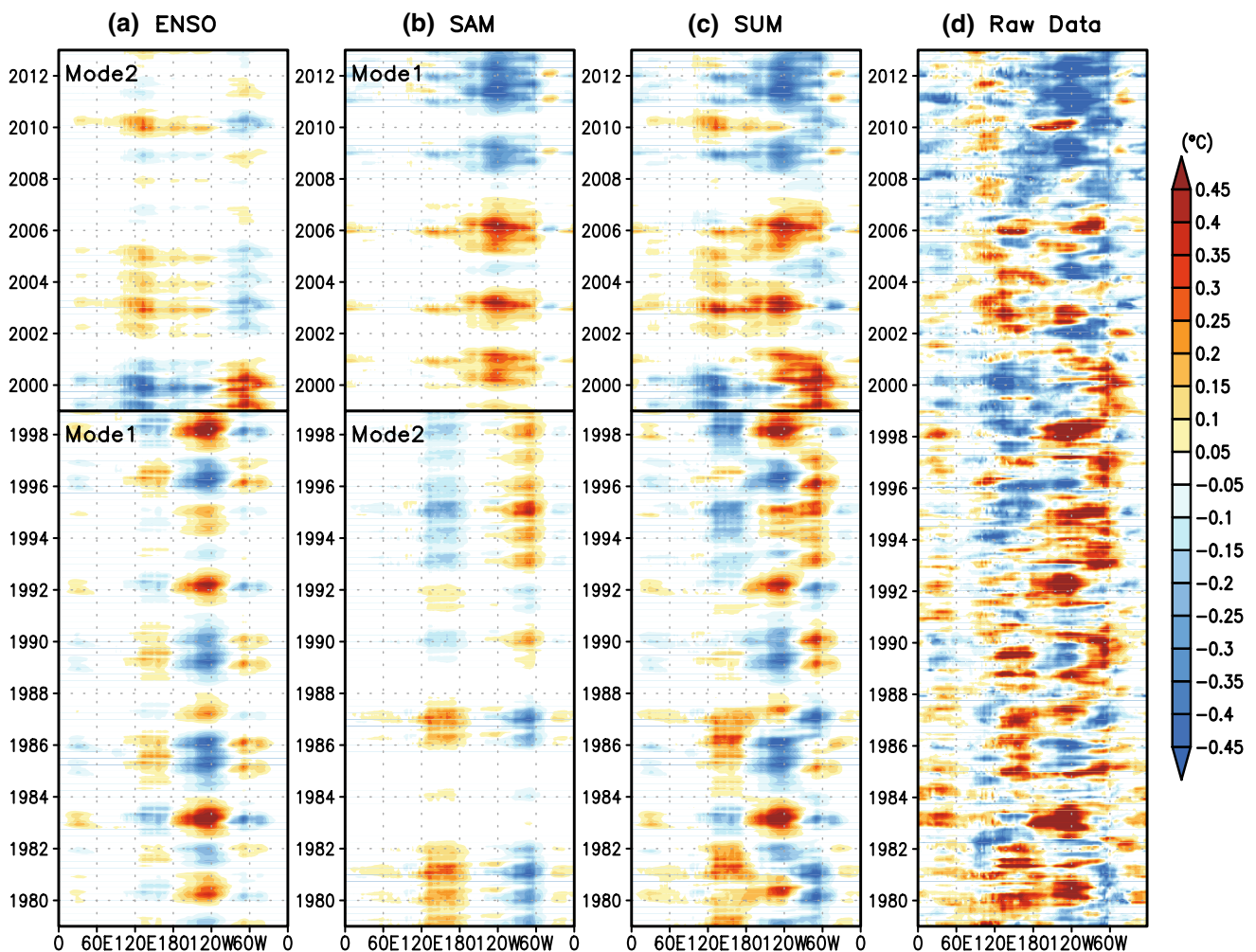
Fig. 7 a Longitude–time cross section of the reconstructed SSTA averaged over 60°–70°S based on the first CSEOF mode during the period 1979–1998 and the second CSEOF mode during the period 1999–2012. **b** The same map as in (**a**) but for the second CSEOF mode during the period 1979–1998 and the first CSEOF mode during the period 1999–2012. **c** The sum of the reconstructed SSTA shown in (**a**) and (**b**). **d** Longitude–time cross section of the SSTA of the Extended Reconstruction SST version 3 raw data

period, the SSTA displayed a dipole structure that centered over the western Pacific and the Drake Passage (Fig. 7a). It should be noted that each El Niño/La Niña event was well reflected in the reconstructed SSTA. For example, Fig. 7a depicts amplified SSTA during strong El Niño years of 1982–1983 and 1997–1998. The signatures of CP El Niño during the 2000s, that is, 2001–2002, 2002–2003, 2004–2005, and 2009–2010 (Kug et al. 2009; Yeh et al. 2009), can also be traced in the reconstructed SSTA. Meanwhile, the SAM-related SSTA pattern in Fig. 7b displays a dipole-like structure that centers over the western Pacific and the Drake Passage in the first period. In the second period, however, maximal SSTA variability occurred over the Amundsen and Bellingshausen Seas. It is noteworthy that the SAM-related modes exhibited distinct phase transitions during both periods. The phase transition in the first period occurred in 1988–1989 from a negative to a positive phase

of the SAM and in 2006–2007 in the second period. Earlier studies have reported decadal changes of the SAM between the 1980s and the 1990s, which modulated the observed SH climate variability (Fogt and Bromwich 2006; Fogt et al. 2011; Stammerjohn et al. 2008).

We then assessed the role of the ENSO- and the SAM-related SSTA extracted by the CSEOF modes in explaining the observed total SST variability. For a comparison, the longitude–time cross sections of the combined SSTA for the two modes and the raw data are presented respectively in Fig. 7c, d. A visual inspection of the two sections indicates that the two modes together reasonably reproduced the main features of the observed SSTA, particularly over the Pacific sector. A quantitative comparison via correlation analysis confirms the similarity of the two sections; correlations over the Pacific region (averaged over 160°–260°E) were 0.70 and 0.83 for the first and the second periods,

respectively. This indicates that the SAM and the ENSO are the two dominant modes driving SH SST variability.

Considering that the first CSEOF mode of SSTA changed from the ENSO mode in the first period into the SAM mode in the second period, the overall features in the two-mode reconstruction and the raw data (Fig. 7c, d) generally reflect the ENSO characteristics in the first period (Fig. 7a, c) and the SAM characteristics in the second period (Fig. 7b, c). That is, the SH SST variability was largely affected by the ENSO in the first period but was largely affected by the SAM in the second period. For example, SST variability around the Ross Sea (180°–120°W) in the first period is practically in accord with the ENSO-related SST variability because the SAM-related SST variability was obscure in this region. On the contrary, the pattern of total SST variability in the second period appeared to be strongly influenced by the SAM. In accordance with the phase of the SAM, positive SSTA was dominant in 1999–2006, and negative SSTA was dominant in 2007–2012 over the high-latitude SH Ocean. In particular, the overall cooling of SST in recent years appears counterintuitive to the ongoing increase in the concentration of atmospheric greenhouse gases. The cause of this SST cooling remains a matter of debate with diverse perspectives on anthropogenic and natural climate variability factors. It can be inferred from Fig. 7, however, that the cold SSTA in the SH during the late 2000s originated mainly from the SAM variability, which is associated primarily with the atmospheric and oceanic internal dynamics (Sen Gupta and England 2007; Thompson and Wallace 2000).

6 Discussion and concluding remarks

Decadal change in the SH climate occurred in the late 1990s in association with the two leading modes, ENSO and the SAM, which we have investigated by using CSEOF and regression analyses. Linear regression using the ENSO and SAM indices also results in patterns similar to those in the present study and confirms that SH SST and geopotential height anomalies are significantly different before and after the late-1990s. The remarkable change in the SH high-latitude ENSO teleconnection was primarily due to the structural change of ENSO from the EP type into the CP type in the late 1990s. During 1979–1998 (the first period), the atmospheric variability associated with EP-type ENSO was characterized by the PSA pattern, which implies teleconnection from the tropical Pacific via Rossby wave propagation. Local changes in the turbulent and Ekman heat fluxes in accordance with this atmospheric PSA pattern, in turn, led to the changes in SST. During 1999–2012 (the second period), however, the dominant mode of ENSO featured maximal warming in the CP region, and the related

SH atmospheric and oceanic variability consequently differed significantly from that in the first period. In particular, the intensity and persistence of the PSA pattern was weaker in the second period; the PSA-like structure appeared only during the austral spring, and the high-latitude zonal wave structure was favored during the austral autumn and winter. Although the physical relationship between the classical type of ENSO (EP) and the SH atmospheric and oceanic variability is well established in earlier studies (e.g., Harangozo 2000; Mo and Paegle 2001; Turner 2004; Yuan 2004), the impacts of the new type of ENSO (CP) on the SH climate is still not fully understood. Several recent studies have investigated the SH climate variability associated with CP El Niño (Ding et al. 2011; Lee et al. 2010; Song et al. 2011), but there is no clear consensus on the physical mechanism linking CP El Niño and the SH atmospheric and oceanic circulations. The present study also examined the CP El Niño-related SH climate variability based on statistical analysis. Further investigation based on coupled ocean–atmosphere models, however, is needed to identify the detailed physical mechanism of the SH high-latitude response to CP El Niño. Understanding this physical mechanism is an important step for predicting future climate in the SH considering that CP El Niño may occur more frequently than EP El Niño under the projected global warming scenarios (Yeh et al. 2009).

Decadal changes in the SH climate appears to be linked with the SAM as well. Analyses presented in Sect. 4 indicate that the difference in the SSTA pattern in relation to the SAM between the two periods is primarily attributed to the non-annular spatial component of the SAM for the two periods. During the first period, the non-annular component of the pressure pattern associated with the SAM was found over the Bellingshausen and the Weddell Seas, which yielded a dipole-like SST response in the SH high latitudes. During the second period, however, the zonally asymmetric component was found in the eastern central Pacific, which consequently induced SST cooling in the central Pacific. Although the importance of the non-annular component of the SAM in affecting local climate variability was highlighted in earlier studies (Hall and Visbeck 2002; Lefebvre and Goosse 2005; Lefebvre et al. 2004; Limpasuvan and Hartmann 2000; Screen et al. 2009; Stammerjohn et al. 2008), its decadal variability has not been fully documented thus far. Further, it is generally understood that the SAM is modulated largely by global warming with a positive-phase dominance of the SAM under increased greenhouse gas conditions (Cai et al. 2003; Fyfe et al. 1999; Marshall et al. 2004; Miller et al. 2006). However, changes in the specific spatial structure of the SAM in association with global warming are not well understood. Given the importance of the SAM in the SH climate variability in the coming decades, it is imperative to pursue a better understanding of

the decadal change in the SAM, particularly in its spatial structure.

One notable point in the present study is that the dominant mode of SST variability changed from the ENSO in the first period into the SAM in the second period. Further, the first mode (i.e., the ENSO-related mode for the first period and the SAM-related mode for the second period) explains approximately 30 % of the total variance in the raw SST dataset, which is twice as much as that explained by the second mode. This finding reflects that there has been a decadal change in the dominant physical mechanism affecting the SH climate. The cause or reason for this decadal change, however, cannot be investigated in detail in the present study, which, in a large part, is due to the short analysis period. Therefore, future investigation based on model experiments or datasets under the auspices of the Intergovernmental Panel on Climate Change (IPCC) is required to further explore the detailed mechanism of this physical change. Also, studies regarding contribution of global warming or Antarctic sea-ice trends on SH SST variability will provide more accurate understanding of SH climate change.

References

Alexander MA, Bladé I, Newman M, Lanzante JR, Lau NC, Scott JD (2002) The atmospheric bridge: the influence of ENSO teleconnections on air–sea interaction over the global oceans. J Clim 15(16):2205–2231

Ashok K, Behera SK, Rao SA, Weng H, Yamagata T (2007) El Niño Modoki and its possible teleconnection. J Geophys Res 112:C11007. doi:10.1029/2006JC003798

Bond N, Overland J, Spillane M, Stabeno P (2003) Recent shifts in the state of the North Pacific. Geophys Res Lett 30(23):2183. doi:10.1029/2007GL031972

Cai W, Whetton P, Karoly DJ (2003) The response of the Antarctic Oscillation to increasing and stabilized atmospheric CO_2. J Climate 16:1525–1538

Ciasto LM, England MH (2011) Observed ENSO teleconnections to Southern Ocean SST anomalies diagnosed from a surface mixed layer heat budget. Geophys Res Lett 38:L09701. doi:10.1029/2011GL046895

Ciasto LM, Thompson DW (2008) Observations of large-scale ocean–atmosphere interaction in the Southern Hemisphere. J Clim 21:1244–1259. doi:10.1175/2007JCLI1809.1

Ding Q, Steig EJ, Battisti DS, Küttel M (2011) Winter warming in West Antarctica caused by central tropical Pacific warming. Nat Geosci 4:398–403. doi:10.1038/NGEO1129

England MH, McGregor S, Spence P, Meehl GA, Timmermann A, Cai W, Sen Gupta A, McPhaden MJ, Purich A, Santoso A (2014) Recent intensification of wind-driven circulation in the Pacific and the ongoing warming hiatus. Nat Clim Change 4:222–227

Fogt RL, Bromwich DH (2006) Decadal variability of the ENSO teleconnection to the high-latitude South Pacific governed by coupling with the Southern Annular Mode. J Climate 19:979–997

Fogt RL, Bromwich DH, Hines KM (2011) Understanding the SAM influence on the South Pacific ENSO teleconnection. Clim Dyn 36:1555–1576

Frankignoul C (1985) Sea surface temperature anomalies, planetary waves, and air–sea feedback in the middle latitudes. Rev Geophys 23:357–390

Fyfe J, Boer G, Flato G (1999) The Arctic and Antarctic Oscillations and their projected changes under global warming. Geophys Res Lett 26(11):1601–1604

Garreaud RD, Battisti DS (1999) Interannual (ENSO) and interdecadal (ENSO-like) variability in the Southern Hemisphere tropospheric circulation. J Clim 12:2113–2123

Gong D, Wang S (1999) Definition of Antarctic oscillation index. Geophys Res Lett 26(4):459–462

Hall A, Visbeck M (2002) Synchronous variability in the Southern Hemisphere atmosphere, sea ice, and ocean resulting from the annular mode. J Climate 15:3043–3057

Harangozo S (2000) A search for ENSO teleconnections in the west Antarctic Peninsula climate in austral winter. Int J Climatol 20:663–679

Harangozo S (2004) The relationship of Pacific deep tropical convection to the winter and springtime extratropical atmospheric circulation of the South Pacific in El Niño events. Geophys Res Lett 31:L05206. doi:10.1029/2003GL018667

Holland MM, Bitz CM, Hunke EC (2005) Mechanisms forcing an Antarctic dipole in simulated sea ice and surface ocean conditions. J Climate 18:2052–2066

Jin D, Kirtman BP (2009) Why the Southern Hemisphere ENSO responses lead ENSO. J Geophys Res 114:D23101. doi:10.1029/2009JD012657

Kanamitsu M, Ebisuzaki W, Woollen J, Yang SK, Hnilo J, Fiorino M, Potter G (2002) NCEP–DOE AMIP-II Reanalysis (R-2). Bull Am Met Soc 83(11):1631–1643. doi:10.1175/BAMS-83-11-1631

Kao HY, Yu JY (2009) Contrasting eastern-Pacific and central-Pacific types of ENSO. J. Climate 22:615–632

Karoly DJ (1989) Southern Hemisphere circulation features associated with El Niño–Southern Oscillation events. J Climate 2:1239–1252

Kidson JW, Renwick JA (2002) The Southern Hemisphere evolution of ENSO during 1981–1999. J Clim 15:847–863

Kim KY, North GR (1997) EOFs of harmonizable cyclostationary processes. J Atmos Sci 54(19):2416–2427

Kim KY, North GR, Huang J (1996) EOFs of one-dimensional cyclostationary time series: computations, examples, and stochastic modeling. J Atmos Sci 53(7):1007–1017

Kosaka Y, Xie SP (2013) Recent global-warming hiatus tied to equatorial Pacific surface cooling. Nature 501:403–407

Kug JS, Jin FF, An SI (2009) Two types of El Niño events: cold tongue El Niño and warm pool El Niño. J Climate 22:1499–1515

Lachlan-Cope T, Connolley W (2006) Teleconnections between the tropical Pacific and the Amundsen-Bellinghausens Sea: role of the El Niño/Southern Oscillation. J Geophys Res 111:D23101. doi:10.1029/2005JD006386

Larkin NK, Harrison D (2005) Global seasonal temperature and precipitation anomalies during El Niño autumn and winter. Geophys Res Lett 32:L16705. doi:10.1029/2005GL022860

Lee T, McPhaden MJ (2010) Increasing intensity of El Niño in the central-equatorial Pacific. Geophys Res Lett 37:L14603. doi:10.1029/2010GL044007

Lee T, Hobbs WR, Willis JK, Halkides D, Fukumori I, Armstrong EM, Hayashi AK, Liu WT, Patzert W, Wang O (2010) Record

warming in the South Pacific and western Antarctica associated with the strong central-Pacific El Niño in 2009–10. Geophys Res Lett 37:L19704. doi:10.1029/2010GL044865

Lefebvre W, Goosse H (2005) Influence of the Southern Annular Mode on the sea ice–ocean system: the role of the thermal and mechanical forcing. Ocean Sci 1:145–157

Lefebvre W, Goosse H, Timmermann R, Fichefet T (2004) Influence of the Southern Annular Mode on the sea ice–ocean system. J Geophys Res 109:C09005. doi:10.1029/2004JC002403

L'Heureux ML, Thompson DWJ (2006) Observed relationships between the El-Niño/Southern Oscillation and the extratropical zonal-mean circulation. J Climate 19:276–287

Li Z (2000) Influence of tropical Pacific El Niño on the SST of the Southern Ocean through atmospheric bridge. Geophys Res Lett 27:3505–3508

Limpasuvan V, Hartmann DL (2000) Wave-maintained annular modes of climate variability. J Clim 13:4414–4429

Mantua NJ, Hare SR, Zhang Y, Wallace JM, Francis RC (1997) A Pacific interdecadal climate oscillation with impacts on salmon production. Bull Am Meterol Soc 78(6):1069–1080

Marshall GJ, Stott PA, Turner J, Connolley WM, King JC, Lachlan-Cope TA (2004) Causes of exceptional atmospheric circulation changes in the Southern Hemisphere. Geophys Res Lett 31:L14205. doi:10.1029/2004GL019952

Mayewski PA, Meredith M, Summerhayes C, Turner J, Worby A, Barrett P, Casassa G, Bertler NA, Bracegirdle T, Naveira Garabato A (2009) State of the Antarctic and Southern Ocean climate system. Rev Geophys 47:RG1003. doi:10.1029/2007RG000231

Merrifield MA, Thompson PR, Lander M (2012) Multidecadal sea level anomalies and trends in the western tropical Pacific. Geophys Res Lett 39:L13602. doi:10.1029/2012GL052032

Miller R, Schmidt G, Shindell D (2006) Forced annular variations in the 20th century intergovernmental panel on climate change fourth assessment report models. J Geophys Res 111:D18101. doi:10.1029/2005JD006323

Minobe S (2000) Spatio-temporal structure of the pentadecadal variability over the North Pacific. Prog Oceanogr 47(2):381–408

Minobe S (2002) Interannual to interdecadal changes in the Bering Sea and concurrent 1998/99 changes over the North Pacific. Prog Oceanogr 55(1):45–64

Mo KC (2000) Relationships between low-frequency variability in the Southern Hemisphere and sea surface temperature anomalies. J Clim 13:3599–3610

Mo KC (2010) Interdecadal modulation of the impact of ENSO on precipitation and temperature over the United States. J Clim 23(13):3639–3656

Mo KC, Higgins RW (1998) The Pacific-South American modes and tropical convection during the Southern Hemisphere winter. Mon Weather Rev 126(6):1581–1596

Mo KC, Paegle JN (2001) The Pacific-South American modes and their downstream effects. Int J Climatol 21(10):1211–1229

Peterson WT, Schwing FB (2003) A new climate regime in northeast Pacific ecosystems. Geophys Res Lett 30(17):1896. doi:10.1029/2003GL017528

Renwick JA (2002) Southern Hemisphere circulation and relations with sea ice and sea surface temperature. J Climate 15(21):3058–3068

Renwick JA, Revell MJ (1999) Blocking over the South Pacific and Rossby wave propagation. Mon Weather Rev 127(10):2233–2247

Rogers JC, Van Loon H (1982) Spatial variability of sea level pressure and 500 mb height anomalies over the Southern Hemisphere. Mon Weather Rev 110(10):1375–1392

Schwing F, Moore C (2000) A year without summer for California, or a harbinger of a climate shift? EOS Trans 81(27):301–305

Screen JA, Gillett NP, Stevens DP, Marshall GJ, Roscoe HK (2009) The role of eddies in the Southern Ocean temperature response to the southern annular mode. J Clim 22(3):806–818

Screen JA, Gillett NP, Karpechko AY, Stevens DP (2010) Mixed layer temperature response to the Southern Annular Mode: mechanisms and model representation. J Clim 23(3):664–678

Sen Gupta A, England MH (2006) Coupled ocean–atmosphere–ice response to variations in the Southern Annular Mode. J Climate 19:4457–4486

Sen Gupta A, England MH (2007) Coupled ocean–atmosphere feedback in the Southern Annular Mode. J Climate 20(14):3677–3692

Simpkins GR, Ciasto LM, Thompson D, England MH (2012) Seasonal relationships between large-scale climate variability and Antarctic sea ice concentration. J Climate 25(16):5451–5469

Smith TM, Reynolds RW, Peterson TC, Lawrimore J (2008) Improvements to NOAA's historical merged land–ocean surface temperature analysis (1880–2006). J Climate 21(10):2283–2296

Song HJ, Choi E, Lim GH, Kim YH, Kug JS, Yeh SW (2011) The central Pacific as the export region of the El Niño–Southern Oscillation sea surface temperature anomaly to Antarctic sea ice. J Geophys Res 116:D21113. doi:10.1029/2011JD015645

Stammerjohn S, Martinson D, Smith R, Yuan X, Rind D (2008) Trends in Antarctic annual sea ice retreat and advance and their relation to El Niño–Southern Oscillation and Southern Annular Mode variability. J Geophys Res 113:390. doi:10.1029/2007JC004269

Taschetto AS, England MH (2009) El Niño Modoki impacts on Australian rainfall. J Clim 22:3167–3174

Thompson DW, Wallace JM (2000) Annular modes in the extratropical circulation. Part I: month-to-month variability. J Clim 13(5):1000–1016

Trenberth KE, Fasullo JT (2013) An apparent hiatus in global warming? Earth's Future 1:19–32

Trenberth KE, Branstator GW, Karoly D, Kumar A, Lau NC, Ropelewski C (1998) Progress during TOGA in understanding and modeling global teleconnections associated with tropical sea surface temperatures. J Geophys Res 103(C7):14291–14324

Turner J (2004) The El Niño–Southern Oscillation and Antarctica. Int J Climatol 24(1):1–31

Verdy A, Marshall J, Czaja A (2006) Sea surface temperature variability along the path of the Antarctic Circumpolar Current. J Phys Oceanogr 36(7):1317–1331

Wallace JM, Gutzler DS (1981) Teleconnections in the geopotential height field during the Northern Hemisphere winter. Mon Weather Rev 109(4):784–812

Weng H, Wu G, Liu Y, Behera SK, Yamagata T (2011) Anomalous summer climate in China influenced by the tropical Indo-Pacific Oceans. Clim Dyn 36(3–4):769–782

Yeh SW, Kug JS, Dewitte B, Kwon MH, Kirtman BP, Jin FF (2009) El Niño in a changing climate. Nature 461(7263):511–514

Yeo SR, Kim KY (2014) Global warming, low-frequency variability, and biennial oscillation: an attempt to understand the physical mechanisms driving major ENSO events. Clim Dyn. doi:10.1007/s00382-013-1862-1

Yeo SR, Kim KY, Yeh SW, Kim W (2012) Decadal changes in the relationship between the tropical Pacific and the North Pacific. J Geophys Res 117:D15102. doi:10.1029/2012JD017775

Yeo SR, Kim KY, Yeh SW, Kim BM, Shim T, Jhun JG (2014) Recent climate variation in the Bering and Chukchi Seas and its linkages to large-scale circulation in the Pacific. Clim Dyn. doi:10.1007/s00382-013-2042-z

Yu L, Weller RA (2007) Objectively analyzed air-sea heat fluxes for the global ice-free oceans (1981–2005). Bull Am Meterol Soc 88(4):527–539. doi:10.1175/BAMS-88-4-527

Yuan X (2004) ENSO-related impacts on Antarctic sea ice: a synthesis of phenomenon and mechanisms. Antarct Sci 16(4):415–425

Yuan X, Yonekura E (2011) Decadal variability in the Southern Hemisphere. J Geophys Res 116:D19115. doi:10.1029/2011JD015673